

Remote Sensing of Water Vapor in the Near IR from EOS/MODIS

Yoram J. Kaufman and Bo-Cai Gao

Abstract—Remote sensing of the total column water vapor (in cloud free conditions) from the proposed MODIS instrument on the NASA's Earth Observing System requires special "water vapor" channels in the near infrared (IR). By using 2 near-IR "water vapor" channels ($0.905\ \mu\text{m}$ and $0.940\ \mu\text{m}$) in addition to existing "window" channels ($0.865\ \mu\text{m}$ and $1.24\ \mu\text{m}$), it will be possible to derive the total column water vapor amount from MODIS data. A ratio of the measured radiance in an absorbing channel at $0.940\pm 0.025\ \mu\text{m}$ or $0.905\pm 0.015\ \mu\text{m}$ to that in a nonabsorbing channel at $0.865\pm 0.020\ \mu\text{m}$ is proposed to retrieve the column water vapor over land.

LOWTRAN-7 code was used to simulate remote sensing of water vapor over 20 different surface covers. The simulation was used to optimize the water vapor channel selection and to test the accuracy of the remote sensing method. The channel selection minimizes the uncertainty in the derived water vapor due to variations in the spectral dependence of the surface reflectance. The selection also minimizes the sensitivity of the selected channels to possible drift in the channel position. In a sensitivity analysis it is shown that the error in the directly derived water vapor amount is $\pm 13\%$. The use of additional MODIS channels reduces the errors due to the effect of haze, subpixel clouds and uncertainties in the temperature profile to $\pm 7\%$. Remote sensing of the variation of water vapor from day to day will be more accurate, because the surface reflectances vary slowly with time. The method was applied to Airborne Visible Infrared Imaging Spectrometer (AVIRIS) data acquired from the NASA-ER2 aircraft and compared with other measurements.

I. INTRODUCTION

Frequent global determination of the distribution of total precipitable water vapor is important to increase the understanding of the hydrological cycle, biosphere-atmosphere interactions, the energy budget, and for monitoring climate change due to the greenhouse gases. For example, climate model calculations have shown that water vapor, a greenhouse gas, generates a positive feedback that accelerates the warming trend due to CO_2 and other greenhouse gases, and therefore increasing the climatic impact of fossil fuel consumption [3], [25]. The complex interaction between water vapor, aerosol, and clouds makes it very difficult to quantify the water vapor feedback without further systematic measurements of water vapor, aerosol, and clouds [32]. It is interesting to monitor the spatial variability of water vapor down to the cloud scale, as shown from aircraft measurements [16]. It is of particular importance to monitor seasonal and annual changes in the precipitable water on regional scales in order to monitor

drought conditions and desertification processes. The sparse location of ground monitoring stations, especially in dry areas, calls for an accurate remote sensing technique that can provide water vapor information on a daily basis with a high spatial resolution (e.g., 1–5 km from MODIS).

Present infrared sounders [4], [5], [22], [29] are capable of retrieving water vapor profiles as a byproduct of remote sensing of the atmospheric temperature profiles. The derived water vapor profile depends in part on the initial guess for the temperature and moisture profiles assumed in the inversion [14], being particularly sensitive to the assumed profiles close to the surface [27]. As far as we know, no systematic comparison between total precipitable water vapor derived by inversion of the HIRS/MSU data and radiosonde measurements has yet been published. Unpublished data (Susskind, private communication) indicates absolute accuracy of 20%. Recently collected radiosonde (21 cases) and sunphotometer (57 cases) measurements of total precipitable water over the Sahel [13] in Africa, indicate virtually no correlation (r^2 between 0.01 and 0.28) with precipitable water derived from HIRS/MSU [17]. A similar approach which alternatively uses microwave data over the oceans is able to retrieve water vapor amounts with errors of the order of 10% [23]. This method has not been applied over land due to the variability of the land microwave emissivity.

Chesters *et al.* [4] retrieved precipitable water vapor from the VISSR Atmospheric Sounder, using an *a priori* estimate of the mean air temperature from radiosonde data. With this temperature estimate they found a correlation, r , between the derived water vapor and the radiosonde measurements of $r = 0.27$ in one case and 0.43 in a second case, with an RMS error of $1\ \text{g/cm}^2$ in both cases. Kleespies and McMillin [22] developed a split window technique that utilizes temperature variation in a heterogeneous terrain. They found a correlation above 0.7 between the *in situ* and retrieved water vapor. For water derived from the AVHRR the standard error was $0.4\ \text{g/cm}^2$. Due to these difficulties with the remote sensing techniques, Birkenheuer [1] renormalized retrieved water vapor from VISSR-VAS by microwave measurements of water vapor from the ground. In arid regions where the difference between the surface temperature and the boundary layer temperature is large (e.g., the Sahel region during the afternoon), a high correlation was found between the infrared sensitivity to total precipitable water vapor and sunphotometer measurements of water vapor [17]. The infrared sensitivity to precipitable water vapor used in this case is the difference in the apparent temperature between the $11\text{-}\mu\text{m}$ and $12\text{-}\mu\text{m}$

Manuscript received December 31, 1990; revised September 11, 1991; rerevised February 12, 1992.

Y. J. Kaufman is with NASA/Goddard SFC, Greenbelt, MD 20771.

B.-C. Gao is with CIRES, University of Colorado, Boulder CO 80309-0216.

IEEE Log Number 9200750.

channels of the AVHRR. In other regions the correlation is lower and the slope and intercept are different due to the different surface conditions (Eck and Holben, personal communication).

From theoretical considerations it follows that if the apparent surface temperature (resultant from the actual skin temperature and emissivity) is about equal to the average temperature of the boundary layer, where most of the water vapor usually reside, infrared and microwave remote sensing will not be sensitive to the boundary layer water vapor. In this case, any IR or microwave photon emitted from the surface and absorbed by water vapor in the boundary layer, will be reemitted from the boundary layer, thus having little effect on the upwelling radiance. Therefore, though remote sensing of water vapor from the EOS-AIRS/MHS instrument is expected to yield accurate profiles of water vapor above the boundary layer, it is expected that the transmission of the solar radiation in the near IR will be more sensitive to the total precipitable water vapor.

In this paper, we propose an optical technique that utilizes the solar radiation reflected by the surface for remote sensing of water vapor from the Moderate Resolution Imaging Spectrometer (MODIS) onboard NASA's planned Earth Observing System. The technique can be applied to images acquired over land areas over cloud free pixels. A difference between the total precipitable water derived from the near-IR MODIS-N channels and the water vapor in the upper layers of the atmosphere derived from the IR and microwave channels on AIRS/MHS or MODIS will enable an accurate estimate of the water vapor in the boundary layer. This will enable the study of the interaction of water vapor with the earth's vegetation, soils and inland water bodies, with atmospheric aerosol and clouds. Remote sensing from MODIS will enable the determination of water vapor with spatial resolution of 1–5 km.

Remote sensing of water vapor from ground-based transmission measurements in and around the near IR absorption bands has been reported [6], [11], [26], [35]. These measurements were based on observations of the transmitted sun light in a channel that corresponds to the water vapor absorption band ($0.94\ \mu\text{m}$) and nearby channels in atmospheric windows ($0.87\ \mu\text{m}$ and $1.03\ \mu\text{m}$, [26]). Column water vapor has also been retrieved from high spectral resolution (10 nm) aircraft measurements [33] of reflected solar radiation near $1\ \mu\text{m}$ [10]. The column water vapor is derived by performing a curve fitting of the observed spectra, with calculated spectra in the $0.94\text{-}\mu\text{m}$ and $1.14\text{-}\mu\text{m}$ water vapor band absorption regions with a nonlinear least squares techniques. The precision of the retrieved column water vapor is 5% or better for small concentrations of atmospheric aerosol. This technique is applicable to High Resolution Imaging Spectrometer (HIRIS) [12].

A differential absorption technique for remote sensing of water vapor from space was suggested by Frouin *et al.* [8], [9]. In this technique, two water vapor channels centered at the same wavelength of $0.94\ \mu\text{m}$ but having different widths (of 17 nm and 45 nm) were selected. The two channels have different sensitivities to changes in the amount of atmospheric water vapor. The ratio of the radiances from the two channels is nearly independent of the surface reflectances. The derived

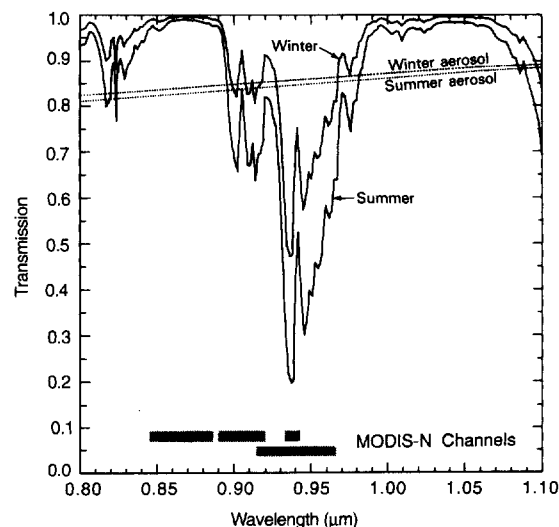


Fig. 1. Spectral transmission of the midlatitude winter and summer atmospheres in the presence of water vapor (solid lines) and aerosols (dashed lines). Computations were performed using the LOWTRAN-7 model, for a slant path through the atmosphere of 45° . The shaded rectangles in the bottom of the figure show the location of the MODIS-N water vapor channels and of the window channel that are used in the analysis.

total amount of water vapor from the channel ratio has a precision of approximately 15%.

The MODIS instrument [28] has a substantially lower spatial and spectral resolution (spatial resolution of 1 km) than the HIRIS instrument (continuous spectrum with 30-m resolution — [12]), but as a result will have a frequent global coverage. Water vapor has a high spatial and temporal variability; therefore, in order to study the biosphere-atmosphere interaction and its relation to global change, global maps of water vapor distribution should be generated, with a 1–5 km resolution on a daily basis or every 2–3 days. For this purpose two new channels were selected for MODIS-N instrument, designed specifically to monitor the global distribution of water vapor, over the land in cloud-free conditions. On MODIS-N a narrow channel at $0.935\ \mu\text{m}$ was also selected, for monitoring water vapor in clouds (Arking, private communication). Over the oceans water vapor can be measured with this technique only for viewing close to the principal plane in the ocean specular reflection, where glint reflection is present. In this paper, we discuss the selection of spectral channels in the near IR which are to be employed for the derivation of total column water vapor.

II. REMOTE SENSING OF WATER VAPOR IN THE NEAR IR

The remote sensing method is based on detecting the absorption by water vapor of the reflected solar radiation as it is transferred down to the surface and up through the atmosphere. The total vertical amount of water vapor can be derived from a comparison between the reflected solar radiation in the absorption band, and the reflected solar radiation in nonabsorbing bands (see Fig. 1). The main uncertainty in the determination of water vapor is in the prediction of the surface reflectance in the absorption band. For surfaces with weak spectral dependence, the surface reflectance in

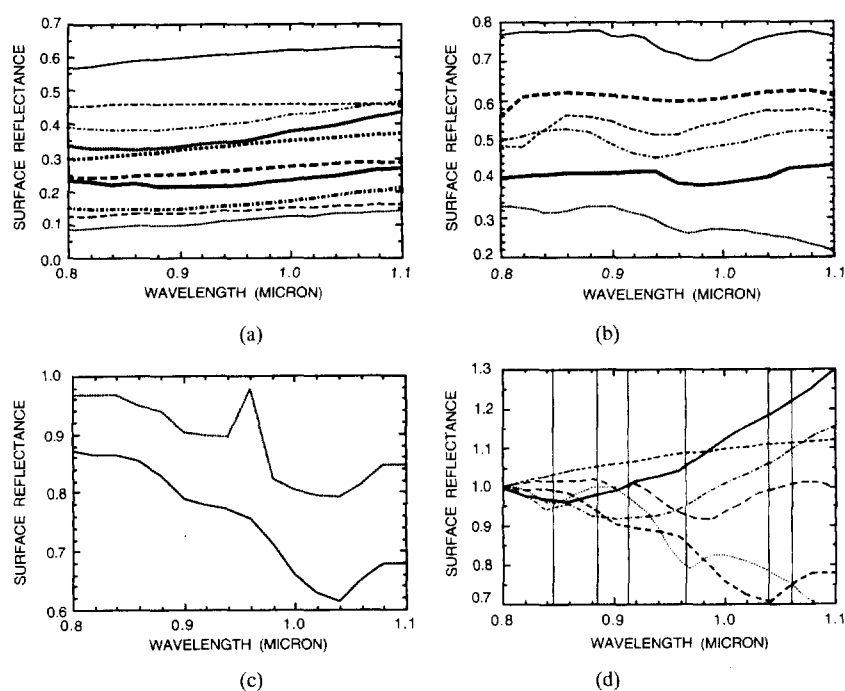


Fig. 2. The main spectra that were used in the simulation of remote sensing of water vapor from MODIS. (a) Soils, from top to bottom on the left side of the figure (after Bowker *et al.*, [2]): silica sand, Chilean nitrates, dry red clay, dry clay soil, dry sandy soil, sand, wet red clay, wet clay soil, wet sandy soil, and soil. (b) Vegetation, from top to bottom (after Bowker *et al.* [2]): red pine needles, ponderosa pine needles, wheat, young wheat, mature wheat. (c) Snows, from top to bottom (after Bowker *et al.* [2]): snow, fresh snow. (d) Normalized spectra, from top to bottom on the right side of the figure (after Bowker *et al.* [2]): dry clay soil, wet red clay, silica sand, red pine needles, snow, grass.

the absorption band can be estimated from its values in the nonabsorbing bands (or one band), and the water vapor content can be estimated from the measured radiance in the absorbing channel. For a complex and variable surface reflectance spectrum, more window channels are required to “predict” the surface reflectance in the water absorption channel, and less accuracy can be expected. The selection of water vapor channels for MODIS is particularly difficult, since a minimum number of special water vapor channels should be used. In Fig. 1 the atmospheric transmission in the $0.8\text{ }\mu\text{m}$ – $1.1\text{ }\mu\text{m}$ range is plotted for two atmospheric models with different amounts of water vapor. Note the location of the atmospheric windows in the $0.86\text{ }\mu\text{m}$ and $1.05\text{ }\mu\text{m}$ region. The rich water vapor spectrum offers a variety of possibilities, from a strong absorption in a narrow channel around $0.935\text{ }\mu\text{m}$ (used on MODIS to detect water vapor in clouds), to more moderate absorption around 0.95 – $0.97\text{ }\mu\text{m}$ and to a weaker absorption around $0.91\text{ }\mu\text{m}$.

Remote sensing of water vapor can be based on a ratio of absorbing to nonabsorbing channels (e.g., a ratio of the measured radiation at $0.94\text{ }\mu\text{m}$ to that at $0.86\text{ }\mu\text{m}$), or on a ratio of a strongly absorbing channel (e.g., a narrow channel centered at $0.94\text{ }\mu\text{m}$) to a moderately absorbing channel (e.g., a wide channel centered at $0.94\text{ }\mu\text{m}$). We have found that the later technique, proposed by Frouin *et al.* [8] reduces significantly the effect of surface reflectance on the channel ratio, but also reduces significantly the sensitivity of the channel ratio to water vapor. A detailed comparison between this method and the methods suggested for MODIS-N is described in Section II.F.

A. Surface Characteristics and the Remote Sensing Technique

Surface reflectance spectra have been reviewed by Bowker *et al.* [2]. This reference provides a wide selection of surface spectra in a numerical form that can be easily implemented for remote sensing simulations. Figs. 2(a–c) shows the main spectra (in the $0.8\text{ }\mu\text{m}$ – $1.1\text{ }\mu\text{m}$ range) that were chosen for the simulation in this paper. In Fig. 2(d) selected spectra were normalized, by dividing the spectral reflectance by the reflectance at $0.8\text{ }\mu\text{m}$. For some surface covers (e.g., silica soil) the reflectance varies almost linearly with wavelength. For this type of cover the best remote sensing technique can be based on a linear interpolation of the surface reflectance between two channels around the water vapor absorption channel. For other surface covers (e.g., dry clay, wet red clay) the reflectance at $0.94\text{ }\mu\text{m}$ is similar to the reflectance at $0.86\text{ }\mu\text{m}$ and much higher at $1.05\text{ }\mu\text{m}$. Therefore, an assumption that the surface reflectance at $0.86\text{ }\mu\text{m}$ is equal to the reflectance at $0.94\text{ }\mu\text{m}$ would be better in this case. Other surface covers have rather erratic reflectance in this spectral range (e.g., red pine needles), and may cause larger errors in remote sensing of the water vapor in any approach. It should be noted that it is anticipated that some errors are present in the spectra compiled by Bowker *et al.* [2]. For example, the reflectance spectra of different kinds of fresh leaves should have liquid water absorption bands centered around $0.99\text{ }\mu\text{m}$. Fig. 2(b) indicates, however, that the location of the water spectral features varies from 0.94 to $0.99\text{ }\mu\text{m}$. Despite this inconsistency, the spectra compiled by Bowker *et al.* [2] provide a starting basis for taking account of surface reflectances on the remote sensing technique.

TABLE I
SURFACE REFLECTANCES (AFTER BOKER *ET AL.*, [2]) AND RATIOS:
 $R_1 = \rho_{0.94}/\rho_{0.86}$, $R_2 = \rho_{0.94}/(0.6\rho_{0.86} + 0.4\rho_{1.05})$, AND $R_3 = \rho_{0.94}/(0.8\rho_{0.86} + 0.2\rho_{1.24})$

SURFACE COVER / WAVELENGTH (μm)	SURFACE REFLECTANCES				REFLECTANCE RATIOS		
	0.86	0.94	1.05	1.24	R_1	R_2	R_3
vegetation							
BARLEY	0.298	0.288	0.319	0.276	0.966	0.940	0.981
BEAN LEAF	0.419	0.416	0.414	0.412	0.993	0.998	0.996
DEHYDRATED BEAN LEAF	0.409	0.408	0.408	0.406	0.998	0.999	0.999
BEANS	0.366	0.351	0.368	0.315	0.959	0.957	0.987
COTTON	0.541	0.537	0.530	0.492	0.993	1.001	1.011
FALLOW FIELD	0.267	0.257	0.226		0.963	1.026	
OATS	0.250	0.236	0.251	0.236	0.944	0.942	0.955
WHEAT	0.547	0.514	0.571	0.506	0.940	0.923	0.954
MATURE WHEAT	0.275	0.275	0.309	0.324	1.000	0.953	0.966
WHEAT STUBBLE	0.233	0.223	0.205		0.957	1.005	
BIRCH LEAVES	0.687	0.699	0.708	0.662	1.017	1.005	1.025
ELM	0.458	0.458	0.458	0.447	1.000	1.000	1.005
SILVER MAPLE	0.500	0.494	0.500	0.487	0.988	0.988	0.993
OAK	0.622	0.635	0.676		1.021	0.987	
LIVE OAK	0.343	0.328	0.369	0.289	0.956	0.928	0.987
DEAD PENDEROSA NEEDLES	0.559	0.611	0.653		1.093	1.024	
PENDEROSA PINE NEEDLES	0.616	0.599	0.620	0.526	0.972	0.970	1.002
RED PINE	0.775	0.744	0.764		0.960	0.965	
RED SPRUCE	0.769	0.725	0.838		0.943	0.910	
GRASS	0.319	0.291	0.251		0.912	0.997	
GRASS	0.658	0.639	0.670	0.554	0.971	0.964	1.003
PRICKLY PEAR	0.217	0.172	0.190	0.110	0.793	0.834	0.879
AVERAGE VEGETATION	0.460	0.450	0.468	0.403	0.970	0.969	0.983
SD VEGETATION	0.177	0.180	0.197	0.144	0.054	0.044	0.035
soils							
BASALT	0.217	0.214	0.211	0.231	0.986	0.997	0.974
GRAY BASALT	0.182	0.161	0.153	0.172	0.885	0.945	0.894
RED CLAY	0.380	0.396	0.444	0.519	1.042	0.976	0.971
WET RED CLAY	0.214	0.217	0.219	0.302	1.014	1.005	0.937
QUARTZ	0.250	0.253	0.262	0.290	1.012	0.993	0.981
GRANITE	0.492	0.491	0.513	0.548	0.998	0.981	0.976
GRAVEL	0.325	0.309	0.303	0.390	0.951	0.977	0.914
LIMESTONE	0.353	0.373	0.402	0.453	1.057	1.001	1.000
UNALTERED ROCK	0.276	0.276	0.281	0.293	1.000	0.993	0.988
BEACH SAND	0.405	0.417	0.434	0.462	1.030	1.001	1.001
CARBONATE BEACH SAND	0.541	0.553	0.560	0.550	1.022	1.008	1.019
GYPSUM SAND	0.430	0.426	0.456	0.388	0.991	0.967	1.010
DRY SILT	0.482	0.509	0.546	0.597	1.056	1.003	1.008
WET SILT	0.200	0.214	0.235	0.265	1.070	1.000	1.005
SOIL	0.094	0.107	0.131	0.162	1.138	0.983	0.994
SOIL	0.295	0.310	0.331	0.365	1.051	1.002	1.003
DRY CLAY SOIL	0.323	0.343	0.400	0.509	1.062	0.969	0.952
WET CLAY SOIL	0.145	0.154	0.188	0.246	1.062	0.949	0.932
DRY LAKE SOIL	0.292	0.294	0.300	0.311	1.007	0.996	0.994
AVERAGE SOIL	0.310	0.317	0.335	0.371	1.023	0.987	0.977
SD SOIL	0.123	0.126	0.133	0.134	0.053	0.019	0.035
AVERAGE ALL	0.391	0.388	0.407	0.385	0.994	0.977	0.979
SD ALL	0.170	0.169	0.181	0.137	0.059	0.036	0.035

B. Channel Selection

It has been observed that surface covers can have a variety of possible spectral dependencies in the 0.8 μm –1.1 μm spectral range. As a result, it is difficult to derive the best remote sensing approach in a systematic logical way. An empirical approach is used in this paper, based on 41 surface cover spectra, taken from Bowker *et al.* [2]. The reflectances of these surface covers in the water vapor absorption band (0.94 μm) and in nearby atmospheric windows (0.86 μm , 1.05 μm , and 1.24 μm) is tabulated in Table I and plotted in Fig. 3. The ratio of the actual reflectances in 0.94 μm to the predicted reflectance in this band is also tabulated in the table. Three different approaches for the prediction of the surface reflectance in the 0.94 μm band are tested:

1. assuming the reflectance at 0.94 μm equals the reflectance at 0.86 μm ,
2. assuming that the reflectance at 0.94 μm can be linearly interpolated from the reflectance at 0.86 μm and 1.05 μm , and
3. assuming that the reflectance at 0.94 μm can be linearly interpolated from the reflectance at 0.86 μm and 1.24 μm .

The first and last approaches would require only one specialized "water vapor" channel on MODIS at around 0.94 μm ,

since the 0.86- μm and 1.24- μm channels are already included in the MODIS design [28], while the second approach would require two additional channels.

The average and standard deviation of each group of surface covers are also given in Table I. An average ratio different than 1.0 (ratio between the actual reflectance at 0.94 μm and the predicted reflectance) can easily be accounted for, provided the surface covers in Table I do represent the global land covers. In this case, the standard deviation in the reflectances ratio is the remaining cause of errors in the remote sensing technique. All three methods show similar results, with the linear interpolation methods scoring the best (for both 1.05 μm and 1.24 μm) with standard deviation of 0.035 (for all surface covers). The simple two-channel ratioing technique has a standard deviation of 0.059. Therefore, the error due to uncertainty in the surface reflectance, is expected to be half in the linear interpolation techniques from that in the simple ratio technique. It is also concluded that there is no need to add the 1.05- μm channel to the MODIS channels, and the remote sensing technique can be based on a simple reflectance ratio, or on linear interpolation of the reflectance between 0.86 μm and 1.24 μm . It is possible, however, that a different set of surface reflectance spectra, would result in somewhat different results. Due to the small difference between the performances of these

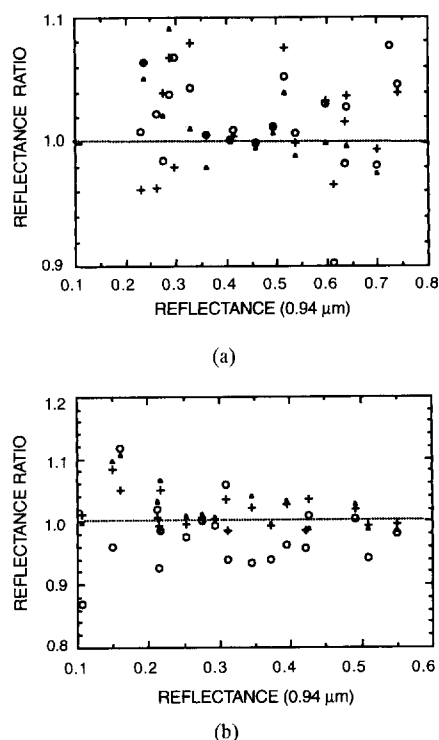


Fig. 3. Ratio between the actual reflectance in the 0.94- μm channel and the predicted reflectance in this channel, as a function of the reflectance in the 0.94- μm channel. (o) — assuming that the reflectance at 0.94 μm is equal to the reflectance at 0.86 μm , (+) — assuming that the reflectance at 0.94 μm can be linearly interpolated between the reflectance at 0.86 μm and the reflectance at 1.05 μm , (D) — assuming that the reflectance at 0.94 μm can be linearly interpolated between the reflectance at 0.86 μm and the reflectance at 1.24 μm . (a) Vegetation surface covers. (b) Soil surface covers.

techniques, and the simplicity of the simple ratio technique, we shall concentrate on the simple ratio method. The apparent reflectance at the top of the atmosphere in a given water vapor band is divided by the apparent reflectance in the atmospheric window, given by the MODIS-N band of 0.845–0.885 μm . A simple remote sensing method can provide a faster operation, as well as smaller errors from other sources like the presence of subpixel clouds, inaccuracies in registrations, etc.

C. Optimization of the Channel Selection

Optimization of the water absorption channel in the 0.94 μm region, is based on the two-channel ratio. Computations of the upward radiance in the two channels are performed using surface reflectance spectra from Bowker *et al.* [2] and the LOWTRAN 7 atmospheric radiance code. This code uses an approximate treatment of multiple scattering to account for aerosol scattering. Fig. 4 shows several options for the channel selection. In this figure, the ratio:

$$T_w(940/865) = \rho_{0.915-0.965}^* / \rho_{0.845-0.885}^* \quad (1)$$

is plotted as a function of the amount of water vapor in the vertical column, where ρ^* is the computed apparent reflectance at the top of the atmosphere for the specified channel. The apparent reflectance is defined as the ratio between the actual upward radiance, and the radiance for a perfect Lambert reflector with reflectance of 1.0 and without the atmosphere. In Fig. 4, the average value and the standard deviation of

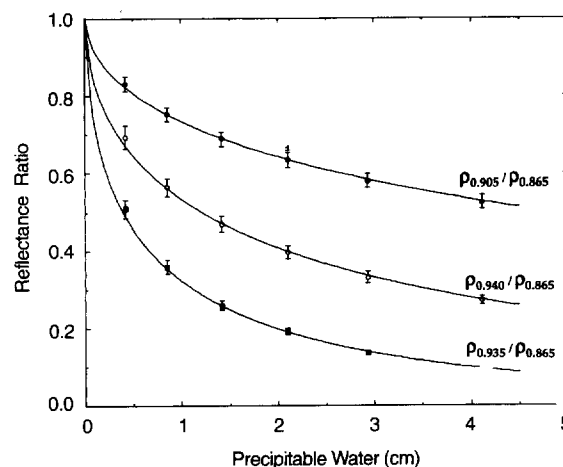


Fig. 4. The dependence of the reflectance ratio T_w , defined as the ratio between the radiance in a water vapor absorbing channel and the radiance in the nonabsorbing channel around 0.865 μm (0.845–0.885 μm), on the amount of water vapor in the vertical column W . (●) — absorbing channel at 0.890–0.920 μm ; (o) — absorbing channel at 0.915–0.965 μm ; (●) — absorbing channel at 0.930–0.940 μm . T_w is computed for 7 vegetation covers, 15 soil covers, and 2 snow covers, all from Bowker *et al.* [2]. The amount of water vapor was varied by using the six atmospheric models of LOWTRAN-7. The solar zenith angle is 40° and the view is at nadir. The amount of water vapor in the atmosphere for each atmospheric model was taken from Tanré *et al.* [31]. The solid lines are the best exponential fits to T_w as a function of \sqrt{W} (4).

T_w is plotted for 7 vegetation covers, 15 soil covers, and 2 snow covers, all from Bowker *et al.* [2]. The amount of water vapor was varied by using the six atmospheric models of LOWTRAN 7 from 0.4 cm of water vapor for subarctic winter atmosphere to 4.1 cm for tropical atmosphere. The amount of water vapor in the atmosphere for each atmospheric model was taken from Tanré *et al.* [30]. Note that the variation of atmospheric models involves also variations in other atmospheric parameters (e.g., temperature profile), thus simulating natural atmospheric variability. For comparison the ratio T_w is also plotted for a less absorbing channel at 0.890–0.920 μm :

$$T_w(905/865) = \rho_{0.89-0.92}^* / \rho_{0.845-0.885}^* \quad (1')$$

a strong absorption channel at 0.930–0.940 μm

$$T_w(935/865) = \rho_{0.93-0.94}^* / \rho_{0.845-0.885}^* \quad (1'')$$

These channels were also selected for MODIS and will be discussed in the next section.

Optimal channel selection is determined by minimizing errors in T_w due to the uncertainty in the surface cover ΔT_w . For a given total precipitable water vapor W , the main error in W results from the uncertainty in T_w due to variation in the ratio of the surface reflectances in the two channels and is given by the standard deviation in the value of T_w for all the surface covers $\sigma[T_w]$. This uncertainty (or the noise in T_w) is normalized by the signal, the change in the channel ratio ($T_{w1} - T_{w2}$) for two values of W , W_1 and W_2 . For the range of precipitable water vapor used in the AFGL atmospheric models of LOWTRAN 7 ($W_1=0.4$ and $W_2=4.1$ cm water for the subarctic winter and the tropical atmospheres) the ratio

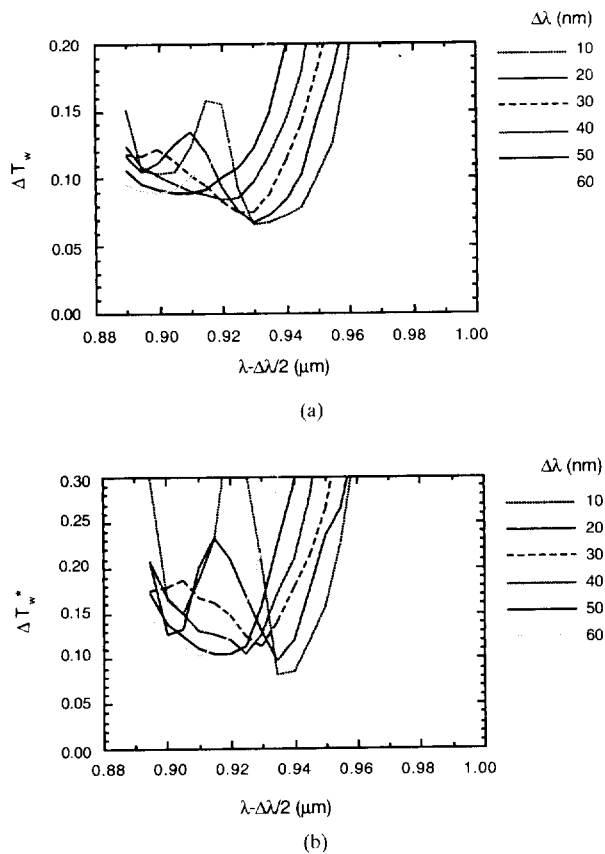


Fig. 5. (a) The dependence of ΔT_w on the spectral location of the lower bound of the water vapor spectral channel ($\lambda - \Delta\lambda/2$), for several widths of the absorption channel ($\Delta\lambda = 10$ to 60 nm), where λ is the spectral location of the center of the channel. ΔT_w is defined as the ratio between the error in the water vapor signal to the signal itself, for a variation in the amount of water vapor from 0.4 cm water to 4.1 cm water. (b) Same as in (a) but for the function ΔT_w^* , that includes the effect of a shift in the spectral channel of the water channel.

ΔT_w is given by:

$$\Delta T_w = \frac{\sigma[T_{w(4.1 \text{ cm water})}]}{[T_{w(0.4 \text{ cm water})} - T_{w(4.1 \text{ cm water})}]} \quad (2)$$

where T_{wi} (i stands for the amount of precipitable water vapor) are averaged for all the surface covers. The sensitivity of T_w to smaller changes in the total water vapor are discussed later in the paper in connection to Table III. The dependence of ΔT_w on the selected water vapor channel is shown in Fig. 5(a). In this figure ΔT_w is plotted as a function of the lower bound of the spectral channel ($\lambda - \Delta\lambda/2$), for several widths of the channel ($\Delta\lambda = 10$ to 60 nm), where λ is the spectral location of the center of the channel. For small $\Delta\lambda$ a lower error due to the uncertainty in the surface reflectance — ΔT_w can be achieved.

A second requirement on the channel selection is that it should be rather insensitive to small variations in the spectral response of the remote sensing system. In Fig. 5(b) a second error formula is given, ΔT_w^* , that includes errors due to uncertainty in the location of the spectral channel. In this case, in addition to the error due to uncertainty in the surface reflectance properties, given by $\sigma[T_w]$, the effect of uncertainty in the spectral location has to be introduced in (2). MODIS is expected to have a spectra monitoring device that will be used

to monitor the spectral shift and correct for it. Therefore, it is assumed that the position of the center of the channel can be shifted anywhere between 0 and 5 nm, and its new position can be monitored with an accuracy of ± 1 nm or better. As a result in the definition of ΔT_w^* , the error of a shift of ± 1 nm is simulated by 20% of the error of a shift of 5 nm, thus representing an average error of 1 nm on a spectral band of 5 nm.

$$\Delta T_w^* = \frac{\sigma[T_{w(4.1 \text{ cm water})}] + 0.2\sigma_\lambda[T_{w(4.1 \text{ cm water})}]}{[T_{w(4.1 \text{ cm water})} - T_{w(0.4 \text{ cm water})}]} \quad (3)$$

Here $\sigma_\lambda[T_{w(4.1 \text{ cm water})}]$ is the average error due to a shift in the spectral channel by 5 nm toward higher or lower wavelengths. The plots of ΔT_w and ΔT_w^* in Fig. 5 can be used for the selection of the channel position and width ($\Delta\lambda$). Optimum channel selection should correspond to a minimum value of ΔT_w and/or ΔT_w^* . Based on this criterion the 0.935 – 0.945 μm channel would be selected. The wider channels, though having 20% larger errors in ΔT_w^* than the 10 nm channel, have several advantages not represented in Fig. 5. The higher signal through the wider channel increases the signal to noise ratio (SNR) of the sensor. The signal through the wider channel is not expected to saturate for large amounts of water vapor as a narrow absorption channel would. As a result the 50 nm wide water absorption channel (0.915 – 0.965 μm) was chosen.

As shown in Fig. 4, the relationship between T_w and the total precipitable water vapor (W) can be expressed by an exponential formula. Moreover, due to the saturation of the water vapor absorption [26], a square root of W is used as the independent variable:

$$T_w(940/865) = \exp(\alpha - \beta\sqrt{W}), \quad r^2 = 0.999 \quad (4)$$

where r^2 is the correlation. For a mixture of all surfaces $\alpha = 0.020$ and $\beta = 0.651$. Note that if the surface reflectance would have been spectrally neutral, α would have been $\alpha = 0$. Vegetation covers and soils have different spectral reflectance in the near IR. As a result the coefficient α is different for these two groups of surface covers: $\alpha = 0.012$ for vegetation and $\alpha = -0.040$ for soil. Operational analysis of the MODIS data for the precipitable water vapor can take advantage of the simultaneous remote sensing of global vegetation index, in order to reduce the errors in the derivation, by adjusting the value of the coefficient α . T_w can also be defined as a function of the precipitable water vapor along the optical path, W^* . W^* is related to the total precipitable water vapor W by

$$W^* = W \left(\frac{1}{\cos \theta} + \frac{1}{\cos \theta_o} \right), \quad T_w = \exp(\alpha - \beta\sqrt{W^*}) \quad (5)$$

where θ is the view zenith angle and θ_o is the solar zenith angle. The coefficients for the best fit to T_w as a function of W^* for the MODIS water vapor channels are given in Table II.

D. Remote Sensing in Dry Conditions

The 50 -nm wide, 0.940 - μm channel, was chosen, as an optimal channel for remote sensing of water vapor in the

TABLE II
LEAST SQUARE FIT APPROXIMATION OF THE EXPRESSION $T_w(\lambda_1, \lambda_2) = \exp(\alpha - \beta\sqrt{W^*})$ GIVEN IN EQ. 5, TO THE COMPUTED REFLECTANCE RATIOS. W^* IS THE WATER VAPOR CONTENT IN CM ALONG THE OPTICAL PATH. CHANNEL 1— λ_1 IS THE WATER VAPOR ABSORPTION CHANNEL AND CHANNEL 2— λ_2 IS THE REFERENCE WINDOW CHANNEL. THE VALUES OF W_{opt}^* AND W_{opt} DEFINED IN EQ. (8), ARE THE VALUES OF THE PATH AND TOTAL PRECIPITABLE WATER VAPOR FOR WHICH THE RESPECTIVE VALUE OF β REPRESENTS AN OPTIMAL CHOICE. RESULTS ARE GIVEN FOR NADIR ($\theta=0^\circ$, $\theta_o=40^\circ$) AND OFF-NADIR ($\theta=60^\circ$, $\theta_o=60^\circ$) VIEWS

view	λ_1	λ_2	α	β	correlation	W_{opt}^*	W_{opt}
nadir	0.915-0.965	0.845-0.885	0.036	0.426	0.999	5	2.4
off-nadir	0.915-0.965	0.845-0.885	-0.024	0.342	0.984	8	2.1
nadir	0.890-0.920	0.845-0.885	0.016	0.209	0.997	23	9.9
off-nadir	0.890-0.920	0.845-0.885	-0.003	0.181	0.989	30	7.6
nadir	0.930-0.940	0.845-0.885	0.043	0.760	0.999	1.7	0.7
off-nadir	0.930-0.940	0.845-0.885	-0.110	0.537	0.986	3.5	0.9
nadir	0.930-0.940	0.915-0.965	0.029	0.332	0.997	9	3.9
off-nadir	0.930-0.940	0.915-0.965	-0.060	0.196	0.970	26	6.5

presence of several cm of water vapor. For low water vapor content ($W \ll 1$ cm water), the narrow channel centered at $0.935 \mu\text{m}$ (10 nm wide), originally selected for remote sensing of water vapor in clouds is more sensitive. This can be seen from Fig. 4, which shows the reflectance ratio, $T_w(935/865)$, as a function of the amount of water vapor ($1''$). This channel is recommended to be used in dry conditions. For a very small water vapor content ($W < 0.5$ cm water) the main error in the remote sensing procedure may result from uncertainty in the spectral surface reflectance. To minimize this effect, a ratio of the narrow channel at $0.935 \mu\text{m}$ to the wide channel at $0.940 \mu\text{m}$ can be used, following the technique of Frouin *et al.*, [8]. This procedure is farther discussed in Section II.F. For large amount of water vapor the absorption in the $0.935\text{-}\mu\text{m}$ channel saturates and the sensitivity to water vapor is small.

E. Remote Sensing in Humid Conditions or for Slant Viewing Directions

For water vapor amount much larger than 4 cm or for slant view and illumination conditions, the strong absorption in the proposed $0.915\text{--}0.965 \mu\text{m}$ channel can partially saturate, resulting in lower sensitivity to water vapor. In this case, a water vapor absorption band in a spectral range corresponding to lower absorption (see Fig. 1) should be preferable. The higher amount of water vapor is simulated using a low slant path (solar zenith angle of 60° and view angle of 60°) for 4 cm water. Though for MODIS, solar zenith angles of 60° corresponds to high latitudes, where high amount of water vapor are unlikely, the present simulation accounts for large amounts of water vapor along the optical path and is still represented by the AFGL atmospheric models. The results for the function ΔT_w are plotted in Fig. 6 for three water vapor channels with a 50-nm width, 30-nm width, and 10-nm width, as a function of the location of the water vapor channel. The arrows indicate location of the channels that are selected for MODIS. The value of ΔT_w for the three channels, increases as a function of the wavelength, due to a larger variability of the spectral surface reflectance across a larger spectral range from the nonabsorbing channel at $0.865 \mu\text{m}$. The selected channel at $0.89\text{--}0.92 \mu\text{m}$ for remote sensing of water vapor in humid conditions, is located in spectral region with minimum values of ΔT_w . For this specific wavelength range, the upper and

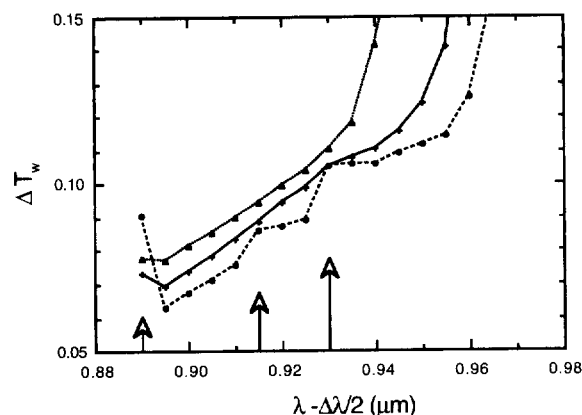


Fig. 6. The function ΔT_w for off nadir view (solar zenith angle of 60° and view angle of 60°) for three water vapor channels with a 50-nm width (Δ), 30 nm width (+) and 10 nm width (\bullet), as a function of the location of the water vapor channel ($\lambda - \Delta\lambda/2$), defined in Fig. 5. The arrows show the location of the selected 30-nm, 50-nm, and 10-nm channels, respectively.

lower bounds of the channel are located in spectral location with minimum water vapor absorption (see Fig. 1), so that small variations in the spectral location of the channel will not generate a substantial change in the reflectance ratio T_w . The dependence of $T_w(905/865)$ on the amount of water vapor is also plotted in Fig. 4. An exponential fit for the relation between T_w and the precipitable water vapor W (cm) is given by expression 4 and tabulated in Table II.

F. Sensitivity of the Water Vapor Channels for Nadir and Off Nadir Viewing

The ratios T_w for the selected channels for nadir and off nadir view are plotted in Fig. 7. Plots are shown for nadir view ($\theta=0^\circ$ and $\theta_o=40^\circ$), and for off nadir view ($\theta=60^\circ$ and $\theta_o=60^\circ$). The coefficients of the exponential fit of T_w as a function of $\sqrt{W^*}$ (5) are given in Table II. The reflectance ratios T_w are larger for off nadir view, resulting in smaller slopes, β , due to the stronger atmospheric effect of aerosol scattering through this longer optical path.

From the analytical relations between T_w and W^* , it is possible to derive the optimum value of β , β_m , that maximizes the sensitivity of the channel ratio for a given range of W^* .

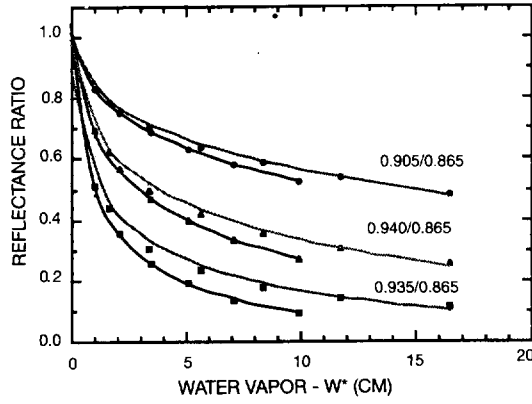


Fig. 7. Same as in Fig. 4 but for nadir view (solar zenith angle of $\theta_o=40^\circ$ — solid black lines) and for slant illumination and view direction ($\theta_o=60^\circ$ and view angle of $\theta_v=60^\circ$ — gray lines) as a function of the amount of water vapor along the optical path W^* .

The sensitivity of T_w to W^* is given by the differential η :

$$\eta(\beta, W^*) = \left| \frac{dT_w}{dW^*} \right| = 0.5\beta T_w / \sqrt{W^*}. \quad (6)$$

The maximum value of η occurs for β_m given by:

$$\left. \frac{\partial \eta}{\partial \beta} \right|_{\beta_m} = 0 \Rightarrow \beta_m = 1/\sqrt{W^*}. \quad (7)$$

Therefore, a channel ratio with a given value of β , optimizes remote sensing of water vapor for a range of column water vapor centered around W_{opt}^* .

$$W_{opt}^* = \beta^{-2}. \quad (8)$$

In Table II the values of W_{opt}^* for each channel ratio are tabulated with the corresponding values of the vertical column water vapor W_{opt} . The three water vapor channels on MODIS do correspond, as expected to separate ranges of water vapor (W_{opt}): under 1 cm — for 0.93–0.94 μm channel, around 2 cm — for 0.915–0.965 μm channel, and around 8 cm of water vapor — for 0.89–0.92 μm channel.

The ratio of the spectral channels suggested by Frouin *et al.* [8] are compared with the performance of the channels selected for MODIS. In this method the channel ratio is computed between a 17-nm channel and a 45-nm channel centered on the 0.94- μm absorption band. Thus the reflectance ratio is between a channel with strong water absorption and a channel with weaker water absorption. The method minimizes the effect of spectral variation of the surface reflectance, but reduces also the sensitivity to water vapor, especially in humid conditions. The slope β for this method was 0.21 for nadir and 0.14 for off-nadir view. A similar method, though with higher values of β , can be applied for MODIS with the ratio of the 0.93–0.94 μm channel to the 0.915–0.965 μm channel (last two lines in Table II). If the spectral characteristics of these two channels are known with high precision, then they are preferable for dry conditions, where the effect of spectral dependence of the surface reflectance may dominant the effect of a smaller dependence on water vapor. For larger amounts of water vapor the fast saturation of this method (see Fig. 7) reduces significantly its accuracy.

III. ACCURACY

In this section several sources of errors in the retrieved water vapor will be discussed. These includes:

1. Uncertainty in the spectral reflectance of the surface.
2. Uncertainty in the sensor calibration.
3. Effect of mixed pixels and clouds.
4. Effect of a shift in the channel location.
5. Uncertainty in pixel registration between several spectral channels.
6. Uncertainty in the atmospheric temperature and moisture profile.
7. Uncertainty in the amount of haze.

The uncertainties are discussed below, and summarized in Table IV.

A. Uncertainty in the Spectral Reflectance of the Surface

The uncertainty in the spectral reflectance of the surface introduces an uncertainty in the reflectance ratio T_w given by ΔT_w . The effect of ΔT_w on the error in the derived water vapor, ΔW , depends on the sensitivity of T_w to water vapor, which in turn depends on the total precipitable water vapor as well as on the channels applied in the reflectance ratio. The value of ΔW can be computed from the differential of T_w as a function of W :

$$\Delta W = \Delta T_w (dT_w/dW)^{-1}. \quad (9)$$

The slope dT_w/dW is computed from the finite difference between the values of T_w between each two atmospheric models with consecutive values of water vapor, W , from $W_1=0.41$ cm for the subarctic winter model to $W_6=4.1$ cm for the tropical model.

$$\Delta W_{ij} = \Delta T_w \frac{W_i - W_j}{T_{wi} - T_{wj}} \quad (10)$$

where the differences are between water vapor content W_i and W_j for consecutive atmospheric models i and j . In Table III the uncertainty ΔW_{ij} is tabulated. The optimum range of the application of each reflectance ratio is indicated in Table III by the lowest values of ΔW .

For nadir view and low water vapor content, the ratio of the narrow to wide absorption channels $T_w(935/940)$ results in smallest errors, followed by the $T_w(940/865)$ ratio. Though $T_w(935/940)$ is less sensitive to variation in surface reflectance properties, the wide 0.94- μm channel should provide a better instrumental signal to noise, and smaller sensitivity to uncertainties in the spectral location. For off nadir view and large water vapor content, the lowest errors are provided by the $T_w(905/865)$ reflectance ratio, due to the weaker absorption in this channel. The uncertainties in ΔW_{ij} in Table III for the selected channel in each range of water vapor content are 6–12%. These errors can be reduced by classification of surface covers and application of the appropriate function $T_w(W)$ for each one. A simple classification, between vegetation and bare soil, can reduce the error by a third, due to the different value of T_w for vegetation and soils (see Section II.C). Alternatively, the error can be also reduced by 50% using the 1.24- μm channel, that reduces the standard deviation in T_w from 0.059 to 0.035

TABLE III
UNCERTAINTIES IN THE DERIVED WATER VAPOR CONTENT ΔW (cm) DUE TO UNCERTAINTY IN THE SPECTRAL REFLECTANCE OF THE SURFACE, FOR FOUR REFLECTANCE RATIOS AND FIVE RANGES OF WATER VAPOR. THE MEDIAN VALUE OF W IS GIVEN FOR EACH RANGE.

channel 1/channel 2 W(cm)	NADIR ($\theta=0^\circ$, $\theta_o=40^\circ$)					OFF-NADIR ($\theta=60^\circ$, $\theta_o=60^\circ$)				
	0.60	1.10	1.80	2.50	3.50	0.60	1.10	1.80	2.50	3.50
0.905/0.865	0.15	0.24	0.33	0.42	0.56	0.09	0.14	0.16	0.21	0.31
0.935/0.865	0.08	0.12	0.14	0.15	0.20	0.06	0.18	0.36	0.71	1.25
0.940/0.865	0.13	0.19	0.26	0.29	0.37	0.08	0.13	0.20	0.34	0.63
0.935/0.940	0.08	0.08	0.07	0.14	0.38	0.10	0.38	0.77	1.67	3.33

(see Table I). The resulting error in remote sensing of water vapor using the additional channels is estimated to be 4–7%. Note that remote sensing of the variation of water vapor from day to day would be more accurate, since usually the surface reflectance varies much slower as a function of time than the amount of water vapor in the atmosphere.

B. Uncertainty in the Sensor Calibration

The columnar amount of water vapor is derived from a ratio or ratios of radiances. Therefore, its accuracy depends on the precision of spectral calibration. The MODIS calibration goals call for spectral precision better than 1.0% at half scale [28]. For a ratio of two channels, a 1% error between spectral channels, corresponds to 1% error in the function T_w and, from (4) and Table II, a 2–4% error in the amount of water vapor. For a three-channel method, the error in T_w , due to uncertainty in the sensor calibration will be somewhat larger: 1.5%, resulting in an error in the water vapor concentration of 3–6%.

C. Effect of Mixed Pixels and Subpixel Clouds

Subpixel clouds affect the derivation of water vapor in two ways: by constituting subpixel elements, and by screening the water vapor located under them. Since most of the water vapor is under the cloud layer, the cloud free water vapor will be underestimated by error equal to the fraction of the pixel occupied by the subpixel clouds. For a 1-km spatial resolution, clouds smaller than 500 m in diameter probably cannot be detected, resulting in an average of 5% in the remaining cloud fraction [34] and a corresponding underestimation of the amount of water vapor of up to 5%. In order to decrease the error resulting from subpixel clouds, the high resolution MODIS channel (250 m) can be used to detect clouds. It is expected that the fraction of undetected clouds in the 250 m channels is less than 1%, and the resulting error in water vapor derived from the 1 km data should be less than 1%.

The effect of subpixel clouds on remote sensing of water vapor depends also on the relationship between the detected radiances and the surface reflectance. If the relationship between the radiance and the surface reflectance would be linear, than the average reflectance (weighted between the subpixel clouds and the surface) could represent the effective reflectance of the pixel. In this case the derived water vapor would represent correctly the average precipitable water vapor above the surface and the subpixel cloud (there is still error due to water vapor screened under the cloud).

Nonlinearity between the apparent reflectance (ρ^*) and the surface reflectance (ρ) arises from multiple reflections between the surface and the atmosphere (s) [7]:

$$\rho^* = \rho_o + t_d t_u \frac{\rho}{1 - s\rho} \quad (11)$$

where ρ_o is the atmospheric reflection function (the apparent reflectance for zero surface reflectance), t_d and t_u are the downward and upward total transmissions through the atmosphere. The nonlinearity in ρ^* is [7]:

$$\frac{\Delta \rho^*}{\rho^*} = s\rho. \quad (12)$$

For $\rho = 0.3$, and a typical value $s = 0.03$ the nonlinearity is around 1%. If the average contrast between the elements that comprise the pixel is around 0.1, the resultant error in the nonlinearity is 0.3%, and the corresponding error in the derived water vapor 0.7%. This small error can be considered as an upper limit to the error estimate.

D. Effect of a Shift in the Channel Location

The effect of a shift in the channel location, can be deduced from the difference ($\Delta T_w^* - \Delta T_w$), each given in Figs. 5(b) and (a), respectively. The relative change in the value of T_w due to a shift of ± 1 nm for the 0.915–0.965 μm channel is ≈ 0.01 . It is expected that the MODIS channels in the near IR will be stable within 1–2 nm (Salomonson, private communication) or that a possible shift in the spectral characteristics of the filter can be detected within 1–2 nm. This uncertainty can correspond to uncertainty in T_w of 0.01–0.02, and in the derived water vapor of 1–2%.

E. Uncertainty in Pixel Registration Between Several Spectral Channels

Errors in pixel registration between the different spectral channels is expected to be smaller than 10% (Salomonson, private communication). This difference may result in a change in the difference between the average reflectance of a pixel between two channels of 0.01, resulting in an error in T_w of $\approx 3\%$, and an error in the derived water vapor of 6–12%. This is a rather large error and can be decreased by averaging a group of pixels (3×3) thus reducing the error to 2–3%.

F. Uncertainty in the Atmospheric Temperature and Moisture Profile

The uncertainty in the relation between the atmospheric temperature profile and the moisture profile may affect the

relationship between the total precipitable water vapor and the vertical transmission. This is due to the dependence of the shape of the water vapor absorption band on temperature. As a result the same amount of water vapor in two layers of different temperatures will have different absorption properties. In order to estimate the effect of this source of error, the transmission through the same total precipitable water vapor was computed (Tanré, private communication) for two atmospheric temperature profiles corresponding to the U.S. standard and Tropospheric model. For the 0.915–0.965 μm channel the transmission of a round trip in the atmosphere, changed from 0.353 to 0.347, and for the 0.89–0.92 μm channel from 0.609 to 0.605. Since T_w is proportional to the transmission, it corresponds to an error in T_w of 1.7% and 0.7%, respectively, and error in the derivation of water vapor of 5% and 2%, respectively. These errors are significant and can be reduced to an error of $\approx 1\%$ by using temperature profile that fits the conditions of measurements, or a profile derived simultaneously from the EOS platform.

G. Effect of Haze Particles

The effect of haze on remote sensing of water vapor depends on the magnitude of the surface reflectance. In Fig. 8 the spectral upward radiance is plotted for two surface covers: a bright grass and a darker clay, and for two concentrations of haze, corresponding to visibilities of 23 km and 5 km for the rural model. In the atmospheric windows haze attenuates reflected solar radiation, thus decreasing the detected radiance. It also scatters direct solar light into the sensor, thus increasing the signal. The net effect of the haze depends on the value of the surface reflectance [7]. For the bright grass — attenuation dominates (Fig. 8(a)), while for the dark clay, the radiance is larger for the hazy conditions due to the dominant scattering effect (Fig. 8(b)). Scattering by the haze particles increases the average path length of photons in the atmosphere, as a result in the water vapor absorption bands there is an increase in the probability of absorption by water molecules. Due to the combination of these three effects, denser haze decreases the radiance in the strong water bands (around 0.94 μm) while increasing the radiation in the less absorbing bands (around 0.905 μm) and in the window bands. As a result neither the three-channel method (were the radiances from the atmospheric windows are interpolated for the water absorption band), nor the two-channel method do eliminate the effect of haze.

In order to find the errors in remote sensing of water vapor, due to uncertainty in the amount of haze, the apparent reflectance is simulated for four LOWTRAN haze models: rural for visibility of 5 km and 23 km, urban for visibility of 5 km, and maritime for visibility of 23 km. In these models, most of the haze and water vapor is located and mixed in the boundary layer. The uncertainty in the visibility, and in the corresponding total vertical burden of the haze, spreads the values of the apparent reflectance ratio, thus doubling the resultant errors. As an example for 4.1 cm of water, the transmission for the four haze models is between 0.26 and 0.31. Note that a reduction to 5-km visibility represents

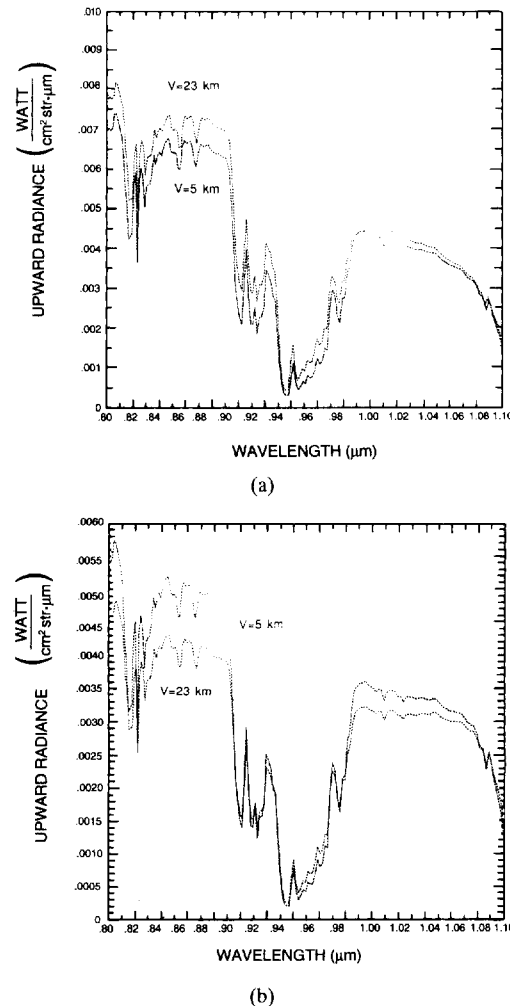


Fig. 8. The spectral upward radiance plotted for two surface covers: (a) bright grass and (b) darker clay, and for two concentrations of haze, corresponding to visibilities of 23 km and 5 km (Midlatitude summer atmosphere).

extreme haze conditions. In most cases the haze variability is much smaller, and may be accounted for, in the "MODIS era," by estimating the amount of haze from the visible and near IR atmospheric windows [18], [31].

For the rural and maritime models the aerosol particles are generated at the Earth's surface, which is also the source of water vapor. Urban or anthropogenic aerosol is generated from gas to liquid chemical conversions in the boundary layer, where the water vapor molecules are of largest concentration. The lifetime of aerosol particles and water vapor are also similar, since both are determined mainly by cloud processes. Therefore, for these models, it is reasonable to assume that the aerosol and water vapor have the same vertical profile. Strong fires [19], [20] and dust storms [24] generate aerosol particles that are injected into layers located above the boundary layer. In this case the different water vapor and aerosol profiles may generate large errors in the retrieved water vapor. The high aerosol layer increases the upward radiance in the water vapor band relative to the radiance in the window bands. As a result the ratio T_w increases, causing an interpretation of a significantly reduced amount of water vapor. Even for a moderate optical thickness of the smoke or dust layers

TABLE IV
ERRORS IN THE DERIVED AMOUNT OF WATER VAPOR FOR NADIR VIEW AND WATER VAPOR AMOUNT OF 4.1 cm. THE ERRORS ARE GIVEN FOR THE DIRECT DERIVATION, USING THE "WINDOW" CHANNEL (0.865 μm), AND THE WATER VAPOR CHANNEL (0.940 μm), AS WELL AS WITH THE ASSISTANCE OF ADDITIONAL MODIS CHANNELS THAT CAN BE USED TO REDUCE THE UNCERTAINTIES.

error source extra	direct derivation	using additional description of the MODIS channels
MODIS channels		
spectral reflectance of the surface	9.0%	5.5%
sensor calibration	3.0%	3.0%
mixed pixels	0.7%	0.7%
subpixel clouds	5.0%	1.0%
shift in the channel location	1.5%	1.5%
pixel registration	2.5%	2.5%
temperature and moisture profile		4.0%
haze effect	6.0%	2.0%
r.m.s. error	13%	7%

TABLE V
COMPARISON BETWEEN WATER VAPOR (cm) DERIVED FROM AVIRIS DATA USING THE TWO-CHANNEL RATIOING TECHNIQUE, THE THREE-CHANNEL RATIOING TECHNIQUE, AND THE CURVE-FITTING TECHNIQUE, TO RADIOSONDE AND MICROWAVE RADIOMETER MEASUREMENTS

Location/ date	In situ instrument	In situ measurement	curve fitting	2 channel ratio	3 channel ratio
Rogers Dry Lake, CA radiosonde Aug. 31, 1988		2.80 \pm 0.2	2.80 \pm 0.09	2.61 \pm 0.2	2.69 \pm 0.1
Platteville, CO March 22, 1990	microwave radiometer	0.69 \pm 0.2	0.67 \pm 0.02	0.58 \pm 0.04	0.69 \pm 0.03
Denver, CO March 22, 1990	microwave radiometer	0.67 \pm 0.2	0.59 \pm 0.03	0.55 \pm 0.05	0.67 \pm 0.03

(optical thickness = 0.2) the apparent precipitable water vapor for the 0.94 μm channel can be lower by 20–25% from the real amount. For the weaker absorption channel (0.905 μm) the effect is lower (5–10%) due to the lower difference between the upward radiance in the absorption band and in the window bands. This erroneous interpretation of precipitable water vapor can be avoided by detection of smoke and dust, as currently planned to be done from MODIS [21]. Substantial difference between the derived water vapor from the two channels, can be also an indication of contamination by high level aerosol.

H. Error Budget

In Table IV, the errors are summarized for nadir view and water vapor amount of 2–4 cm. For off-nadir view or lower amounts of water vapor the errors are larger, as described in the previous section. Note that the use of additional MODIS channels reduces the overall error from 13% to 7%. The precision of remote sensing of water vapor, may be improved, by "calibrating" the surface spectral properties by a comparison of the reflectance ratio used for very dry conditions $T_w(935/940)$ to the reflectance ratio used for normal conditions $T_w(940/865)$. This comparison may result in an update of the coefficient α as a function of location for a given period of time.

IV. APPLICATION TO AVIRIS DATA

In previous sections, simulated radiances with LOWTRAN-

7 using surface reflectance spectra were used to demonstrate the feasibility of a two-channel ratioing technique for remote sensing of water vapor in the near IR from EOS MODIS. In this section, the two-channel ratioing technique is applied to spectral data collected by the Airborne Visible Infrared Imaging Spectrometer (AVIRIS), a precursor to the future satellite instruments, HIRIS. For comparison, a three-channel ratioing technique is also applied to the same data.

AVIRIS images the Earth's surface in 224 spectral channels approximately 10 nm wide, covering the spectral region from 0.4 to 2.5 μm , from an ER-2 aircraft at an altitude of 20 km, with a swath width of approximately 12 km. The ground instantaneous field of view (GIFOV) is 20 \times 20 m. Complete descriptions of the AVIRIS instrument, including radiometric calibration and data processing, are given by Vane [33]. A method for quantitative retrievals of column atmospheric water vapor from AVIRIS data with a spectral curve fitting technique has been described by Gao and Goetz [10].

Several sets of AVIRIS data were used in calculations of two-channel and three-channel ratios. The resulting ratioed images were examined to see the effectiveness of ratioing techniques in removing surface reflectance effects. The locations and dates of the AVIRIS data are given in Table V, together with results from several remote sensing algorithms and *in situ* radiosonde and microwave water vapor radiometer measurements. In the following, the Rogers Dry Lake data set is used as an example to describe the channel ratioing techniques and the methods of retrieving water vapor amounts.

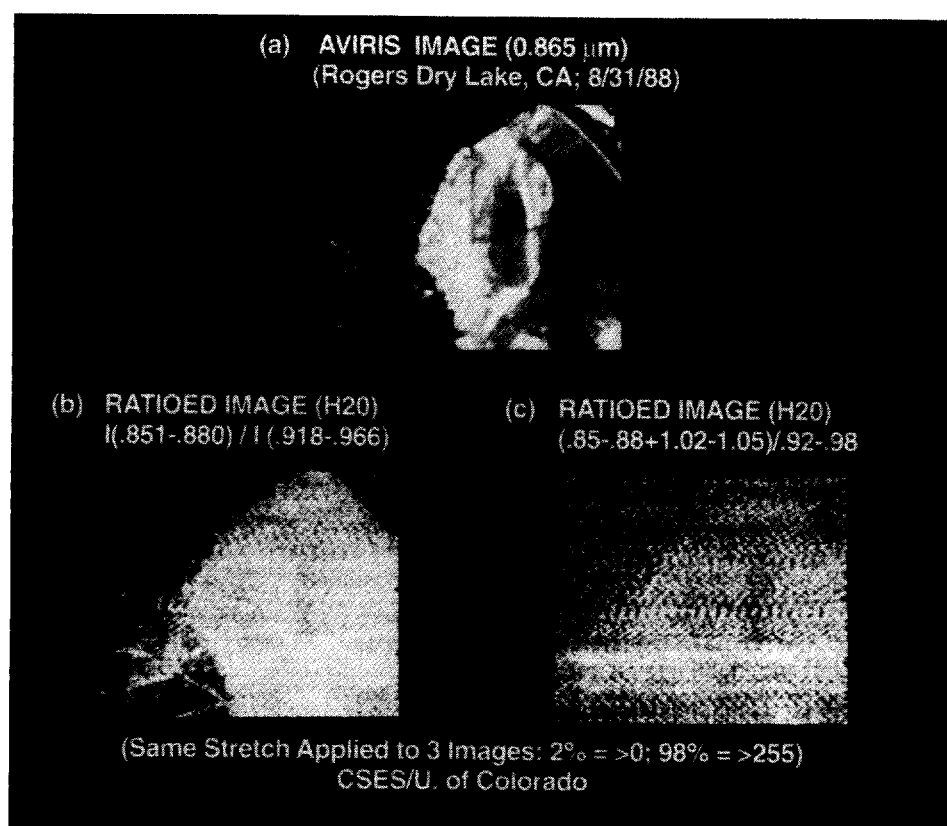


Fig. 9. (a) an image of Rogers Dry Lake, CA processed from radiances of one AVIRIS channel centered at 0.865 μm , (b) a two-channel ratioed image, and (c) a three-channel ratioed image.

Spectra of individual pixels near 1 μm measured over Rogers Dry Lake, have typically SNR's of 50. In order to increase SNR's, the spectral data were averaged on a 4 by 4 pixel basis (16-pixel average). The spatial averaging increases the SNR by a factor of 4 and increases the GIFOV to 80×80 m. Fig. 9(a) shows an image of Rogers Dry Lake. This image was processed from radiance values of one AVIRIS channel centered at 0.865 μm . The brightness over the scene varies significantly because of the very different reflectances of surface targets. The variation of surface elevation over the scene is less than 50 m. In the sites there is no vegetation.

In our data analysis, the AVIRIS radiance spectrum is divided by the solar radiance curve above the atmosphere [15] to remove the effects of the slow variation of solar radiance with wavelength. The resulting spectrum is referred to as the "apparent reflectance spectrum." The apparent reflectances of several AVIRIS 10-nm wide channels were averaged to simulate broader MODIS channels. Specifically, for the two channel ratioing, five AVIRIS channels centered at 0.923, 0.932, 0.942, 0.951, and 0.961 μm were averaged to give one MODIS water vapor channel with a bandpass of 0.918–0.966 μm . The resulting mean apparent reflectance is referred to as ρ_1^* . Three AVIRIS channels centered at 0.856, 0.865, and 0.875 μm were averaged to give one MODIS channel with a bandpass of 0.851–0.880 μm . The resulting mean apparent reflectance is referred to as ρ_2^* . Fig. 9(b) shows the two-channel ratioed image (ρ_1^*/ρ_2^*). The features in this image show much less contrast than those in Fig. 9(a). This demonstrates that the

two-channel ratioing partially removes the surface reflectance effect. The major surface features seen in Fig. 9(a), however, are also seen in Fig. 9(b). This is because the small slopes of spectral reflectance curves of different surface targets are slightly different, and the two-channel ratioing does not allow the complete removal of surface effects. Ideally, if reflectances of different surface targets remain constant in the 0.85–0.97 μm region, the two-channel ratioing would remove the surface effects.

Fig. 10(a) shows the statistical distribution of the two-channel ratioed image. Two peaks are evident. The mean of the ratios is 0.42 and the standard deviation is 0.013. Column water vapor values were derived from the channel ratios using the following methods. A spectrum was first calculated with a spectral model [10], using atmospheric temperature, pressure, and water vapor volume mixing ratioing profiles measured by a radiosonde released one hour prior to the AVIRIS overflight. The spectrum was then convolved with the AVIRIS' instrument function. A channel ratio was calculated from the convolved spectrum. Similar spectra and channel ratios were calculated with different scale factors applied to the water vapor volume mixing ratio profile. A table of channel ratio as a function of column water vapor amount was compiled. Finally, the column water vapor values of the two-channel ratioed image were obtained using a look up table procedure. Table I shows that the mean soil reflectance at 0.94 μm is 2.3% brighter than that at 0.86 μm . This mean spectral dependence of the soil reflectance is taken into consideration,

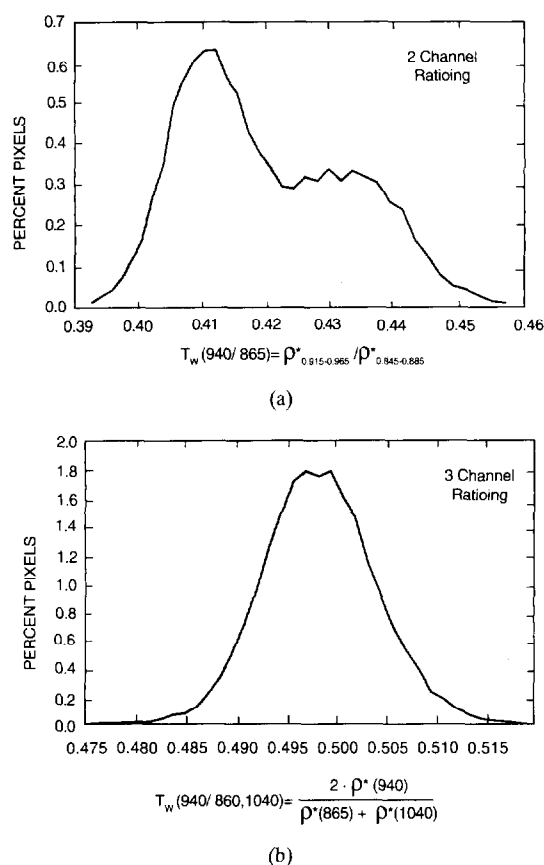


Fig. 10. (a) Statistical distributions of two-channel ratios corresponding to Fig. 9(b), and (b) statistical distributions of three-channel ratios corresponding to Fig. 9(c).

in the derivation of water vapor. The mean column water vapor value for the Rogers Dry Lake AVIRIS scene was 2.61 cm, which is 9% smaller than the 2.8 cm column water vapor value measured with the radiosonde. The standard deviation of water vapor values over the entire scene was 7.5%.

For comparison, column water vapor values were also derived using a three-channel ratioing technique. The methods of channel averages and derivation of water vapor values from three-channel ratioed image are similar to those of two-channel ratioing described above. The three channels ρ'_1 , ρ'_2 , and ρ'_3 , have bandpasses of 0.851–0.880, 0.918–0.985, and 1.023–1.052 μm , respectively. The center of ρ'_2 is located exactly at the midpoint between ρ'_1 and ρ'_3 . Fig. 10(c) shows the three-channel ratioed image $(2\rho'_2)/(\rho'_1 + \rho'_3)$. Surface features are almost indistinguishable in the image. By comparing Fig. 9(c) with Fig. 9(b), it can be seen that the three-channel ratioing does a better job of removing surface features than the two-channel ratioing for the Rogers Dry Lake scene. Fig. 10(b) shows the statistical distribution of the three-channel ratioed image. Unlike Fig. 10(a), the double peak is not obviously present in Fig. 10(b). The mean of the ratios is 0.498 and the standard deviation is 0.006. The mean column water vapor value derived from three-channel ratios is 2.69 cm, approximately 4% smaller than the value measured with the radiosonde. The standard deviation of water vapor values over the entire scene is 3.7%. Table V summarizes the results of the two and three channels ratioing technique for the three

applications of the AVIRIS data, the results from the ground truth (radiosonde or microwave radiometer) as well as the results from the curve fitting technique [10]. The two-channel ratioing technique underestimates the amount of water vapor derived from the ground truth by 0.14 cm in average. Note that the uncertainty in the ground truth itself is 0.1–0.2 cm. The three-channel ratioing technique estimate was lower by 0.11 cm in one case and almost equal to the ground truth in other two cases. Recent comparison between column water vapor measured by 3 radiosondes and a microwave radiometer in Wallops Island, VA (R. Ferrare, private communication) showed an average deviation of $\pm 10\%$ between these four instruments for a range of water vapor of 0.5–2.3 cm.

V. CONCLUSION

The three near-IR water vapor channels on the proposed MODIS instrument on the NASA's Earth Observing System will enable remote sensing of the total column water vapor (in cloud free conditions) with absolute accuracy of $\pm 13\%$, or $\pm 7\%$ if additional MODIS channels are used to decrease the effect of uncertainty in the spectral reflectance of the surface, subpixel clouds, haze and temperature profile on the derived water vapor. A higher precision is expected for monitoring the spatial variability of water vapor and its variation with time. Reflectance ratios for several channel combinations were tested, showing the applicability of each ratio to a given range of the water vapor content. A comparison between the total precipitable water vapor derived from each water vapor channel can be used to the consistency of the remote sensing procedures. The total precipitable water vapor values with global coverage may have important applications in meteorology and hydrology. Combination of the derived total column water vapor, with a resolution of 1–5 km, with remote sensing of other Earth and atmospheric parameters by MODIS, such as temperature, vegetation, clouds and aerosol, will enable an intensive study of the environment and the effect of human activity on climate change.

ACKNOWLEDGMENT

We would like to acknowledge helpful comments from D. Tanré, J. Susskind, and M. D. King, and a thorough review by D. Kratz and R. Frouin.

REFERENCES

- [1] D. J. Birkenheuer, "An algorithm for operational water vapor analyses integrating GOES and dual-channel microwave radiometer data on the local scale," *Appl. Meteorol.*, vol. 30, pp. 834–843, 1991.
- [2] D. E. Bowker, R. E. Davis, D. L. Myrick, K. Stacy, and W. T. Jones, "Spectral reflectances of natural targets for use in remote sensing studies," NASA Reference Pub. 1139, 1985.
- [3] R. D. Cess, G. L. Potter, J. P. Blanchet, G. J. Boer, A. D. Del Genio, M. Deque, V. Dymnikov, V. Galin, W. L. Gates, S. J. Ghan, J. T. Kiehl, A. A. Lacis, H. Le Treut, Z.-X. Li, X.-Z. Liang, B. J. McAvaney, V. P. Meleshko, J. F. B. Mitchell, J.-J. Morcrette, D. A. Randall, L. Rikus, E. Roeckner, J. F. Royer, U. Schlese, D. A. Sheinin, A. Slingo, A. P. Sokolov, K. E. Teylor, W. M. Washington, R. T. Wetherald, I. Yagai, and M.-H. Zhang, "Intercomparison and interpretation of climate feedback processes in 19 atmospheric general circulation models," *J. Geophys. Res.*, vol. 95, pp. 16601–16615, 1990.

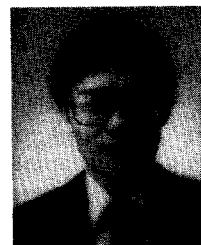
- [4] D. Chesters, L. W. Uccellini, and W. D. Robinson, "Low level water vapor fields from the VISSR atmospheric sounder (VAS) split window channels," *J. Climate Appl. Meteorol.*, vol. 22, pp. 725-743, 1983.
- [5] D. Chesters, L. W. Uccellini, and W. D. Robinson, "A note on optimized retrievals of precipitable water from the VAS split window channels," *J. Climate Appl. Meteorol.*, vol. 26, pp. 1059-1066, 1987.
- [6] F. E. Fowle, "The spectroscopic determination of aqueous vapor," *Astrophys. J.*, vol. 35, pp. 149-162, 1912.
- [7] R. S. Fraser and Y. J. Kaufman, "The relative importance of scattering and absorption in remote sensing," *IEEE Trans. Geosci. Remote Sensing*, vol. 23, pp. 625-633, 1985.
- [8] R. Frouin, P.-Y. Deschamps, and P. Lecomte, "Determination from space of atmospheric total water vapor amounts by differential absorption near 940 nm: Theory and airborne verification," *J. Appl. Meteorol.*, vol. 29, pp. 448-460, 1990.
- [9] R. Frouin and E. Middleton, "A differential absorption technique to estimate atmospheric total water vapor amounts," in *Proc. of the Symposium on the first ISLSCP Field Experiment*, Feb. 7-9, 1990, Anaheim, CA 135-139. Published by the Amer. Meteorol. Soc., 1990.
- [10] B. C. Gao and A. F. H. Goetz, "Column atmospheric water vapor retrievals from airborne imaging spectrometer data," *J. Geophys. Res.*, (Atm.), vol. 95, pp. 3549-3564, 1990.
- [11] D. M. Gates, "Infrared determination of precipitable water vapor in a vertical column of the earth's atmosphere," *J. Meteorol.*, vol. 13, pp. 369-375, 1956.
- [12] A. F. H. Goetz and H. Herring, "The High Resolution Imaging Spectrometer (HIRIS) for EOS," *IEEE Trans. Geosci. Remote Sensing*, vol. 27, pp. 136-144, 1989.
- [13] B. N. Holben and T. Eck, "Precipitable water in the Sahel measured using sunphotometry," *Agric. and Forest Meteorol.*, vol. 52, pp. 95-107, 1990.
- [14] C. M. Hayden, "GOES-VAS simultaneous temperature-moisture retrieval algorithm," *J. Appl. Meteorol.*, vol. 27, pp. 7-5-733, 1988.
- [15] M. Iqbal, *An Introduction to Solar Radiation*. San Diego, CA: Academic, 1983, pp. 43-51.
- [16] G. J. Jedlovac, "Precipitable water estimates from high resolution split window radiance measurements," *J. Appl. Meteorol.*, vol. 29, pp. 863-877, 1990.
- [17] C. O. Justice, T. Eck, D. Tanré, and B. N. Holben, "The effect of water vapor on the NDVI derived for the Sahelian Region from NOAA/AVHRR data," *Int. J. Remote Sensing*, in press, 1991.
- [18] Y. J. Kaufman and C. Sendra, "Algorithm for automatic atmospheric corrections to visible and near-IR satellite imagery," *Int. J. Remote Sensing*, vol. 9, pp. 1357-1381, 1988.
- [19] Y. J. Kaufman, R. S. Fraser, and R. A. Ferrare, "Satellite remote sensing of large scale air pollution — method," *J. Geophys. Res.*, vol. 95, pp. 9895-9909, 1990.
- [20] Y. J. Kaufman, C. J. Tucker, and I. Fung, "Remote sensing of biomass burning in the tropics," *J. Geophys. Res.*, vol. 95, pp. 9927-9939, 1990.
- [21] M. D. King, Y. J. Kaufman, W. P. Menzel, and D. Tanré, "Remote sensing of cloud, aerosol and water vapor properties from the Moderate Resolution Imaging Spectrometer (MODIS)," *IEEE Trans. Geosci. Remote Sensing*, vol. 30, pp. 2-27, 1992.
- [22] T. J. Kleespies and L. M. McMillin, "Retrieval of precipitable water from observations in the split window over varying surface temperatures," *J. Appl. Meteorol.*, vol. 29, pp. 851-862, 1990.
- [23] C. Prabhakara, H. D. Chang, and A. T. C. Chang, "Remote sensing of precipitable water over the oceans from Nimbus 7 microwave measurements," *J. Appl. Meteorol.*, vol. 31, pp. 59-68, 1982.
- [24] J. M. Prospero, R. J. Charlson, V. Mohnen, R. Jaenicke, A. C. Delany, J. Moyers, W. Zoller, and K. Rahn, "The atmospheric aerosol system: an overview," *Rev. of Geophys. and Space Physics*, vol. 21, pp. 1607-1629, 1983.
- [25] A. Raval and V. Ramanathan, "Observational determination of the greenhouse effect," *Nature*, vol. 342, pp. 758-761, 1989.
- [26] J. A. Reagan, K. Thome, B. Herman, and R. Gall, "Water vapor measurements in the 0.94 μ m absorption band: Calibration, measurements and data applications," *Proc. IGARSS*, pp. 63-67, 1987.
- [27] D. Reuter, J. Susskind, and A. Pursch, "First-guess dependence of a physically based set of temperature-humidity retrievals from HIRS2/MSU data," *J. Atmos. Ocean. Tech.*, vol. 5, pp. 70-83, 1988.
- [28] V. V. Salomonson, W. L. Barnes, P. W. Maymon, H. E. Montgomery, and H. Ostrow, "MODIS: Advanced facility instrument for studies of the earth as a system," *IEEE Trans. Geosci. Remote Sensing*, vol. 27, pp. 145-153, 1989.
- [29] J. Susskind, J. Rosenfeld, D. Reuter, and M. T. Chahine, "Remote sensing of weather and climate parameters from HIRS2/MSU on TIROS-N," *J. Geophys. Res.*, vol. 89D, pp. 4677-4697, 1984.
- [30] D. Tanré, C. Deroo, P. Duhaut, M. Herman, J. J. Morcrette, J. Perbos, and P. Y. Deschamps, "Simulation of the satellite signal in the solar spectrum 5S," *Lab. d'Optique Atmos.*, Univers. des Sciences et Techniques de Lille, France, 1986.
- [31] D. Tanré, P. Y. Deschamps, C. Devaux, and M. Herman, "Estimation of Saharan aerosol optical thickness from blurring effects in Thematic Mapper data," *J. Geophys. Res.*, vol. 93, pp. 15955-15964, 1988.
- [32] S. A. Twomey, "Aerosol cloud physics and radiation," in *Seventh Conf. on Atm. Rad.*, AMS, San Francisco, CA, pp. j25-j28, 1990.
- [33] G. Vane, (Ed.), "Airborne visible/infrared imaging spectrometer (AVIRIS)," JPL Pub. 87-38, JPL, Pasadena, CA, 1987.
- [34] B. A. Wielicki and R. M. Welch, "Cumulus cloud properties derived using Landsat satellite data," *J. Climate Appl. Meteorol.*, vol. 25, pp. 261-276, 1986.
- [35] F. E. Volz, "Economical multispectral sun photometer for measurements of aerosol extinction from 0.44 to 1.6 μ m and precipitable water," *Appl. Opt.*, vol. 13, pp. 1732-1733, 1974.



Yoram J. Kaufman received the B.Sc. and M.Sc. degrees in physics from the Technion-Israel Inst. of Technology, Israel, in 1972 and 1974, respectively, and the Ph.D. degree from the Tel-Aviv University in 1979.

He is presently employed at the NASA/Goddard Space Flight Center, Greenbelt, MD, where he began in 1979 on an NRC fellowship award. His current work includes theoretical and experimental research in atmospheric science, radiative transfer, and remote sensing. His research activities include

remote sensing of aerosol and clouds, atmospheric correction of satellite imagery of the Earth's surface, interaction of aerosols and clouds, and their climatic impact, remote sensing of emissions from biomass burning in the tropics, and calibration of satellite sensors. He conducts field experiments that include measurements from aircraft and from the ground of the aerosol properties (smoke aerosol, dust, and anthropogenic aerosol) and their effect on radiative transfer. He is a member of the Earth Observing System—MODIS team. Three of his papers on properties of CO₂ lasers and saturable absorbers, written from his work in the Technion, were selected for the SPIE Milestone Series "of outstanding papers from the world literature on optical and optoelectronic science: Selected Papers on CO₂ Lasers."



Bo-Cai Gao received the B.S. degree from Nankai University in the People's Republic of China in 1982, and the M.S. and Ph.D. degrees from the Ohio State University, in 1984 and 1988, respectively.

He is currently a research associate with the Center for the Study of Earth from Space/Cooperative Institute for Research in Environmental Sciences, University of Colorado at Boulder, where he is conducting research in remote sensing of the lower atmosphere and the surface using the technique of imaging spectrometry. He participated in remote

sensing of upper atmospheric temperatures and vertical distributions of minor and trace gases from high resolution solar occultation spectra collected by the Atmospheric Trace Molecule Spectroscopy (ATMOS) experiment on the Spacelab-3 Shuttle Mission in the spring of 1985.